

# The Abundance of Circumgalactic Medium in TNG100 Stars

DANIEL DEFELIPPIS,<sup>1</sup> SHY GENEL,<sup>2</sup> GREG L. BRYAN,<sup>1,2</sup> DYLAN NELSON,<sup>3</sup> ANNALISA PILLEPICH,<sup>4</sup> AND LARS HERNQUIST<sup>5</sup>

<sup>1</sup>Department of Astronomy, Columbia University, 550 West 120th Street, New York, NY 10027, USA

<sup>2</sup>Center for Computational Astrophysics, Flatiron Institute, 162 Fifth Avenue, New York, NY 10010, USA

<sup>3</sup>Max-Planck-Institut für Astrophysik, Karl-Schwarzschild-Str. 1, D-85741 Garching, Germany

<sup>4</sup>Max-Planck-Institut für Astronomie, Königstuhl 17, D-69117 Heidelberg, Germany

<sup>5</sup>Harvard-Smithsonian Center for Astrophysics, 60 Garden Street, Cambridge, MA 02138, USA

## ABSTRACT

We present a study of the abundance of the circumgalactic medium (CGM) in TNG100, a box of size  $10^2 h^{-1}$  Mpc. We find that the CGM mass is  $\sim 10^{12} M_{\odot}$  at  $z = 0$  and  $\sim 10^{11} M_{\odot}$  at  $z = 5$ . We find that the CGM abundance is  $\sim 1/2$  of the total baryonic mass in the galaxy. The CGM abundance is  $\sim 1/2$  of the total baryonic mass in the galaxy. The CGM abundance is  $\lesssim 10^{12} M_{\odot}$  and is affected by feedback processes. The CGM abundance is  $\lesssim 10^{12} M_{\odot}$  and is affected by feedback processes. The CGM abundance is  $\lesssim 10^{12} M_{\odot}$  and is affected by feedback processes.

*Keywords:* galaxies: abundances, galaxies: evolution, galaxies: formation, galaxies: structure

## 1. INTRODUCTION

The circumgalactic medium (CGM), defined as the gas within the virial radius, is a key component of galaxy evolution. It is the site of star formation, gas accretion, and feedback processes. The CGM is a reservoir of gas that can be used to form stars or be ejected from the galaxy. The CGM is a reservoir of gas that can be used to form stars or be ejected from the galaxy. The CGM is a reservoir of gas that can be used to form stars or be ejected from the galaxy.

The CGM is a reservoir of gas that can be used to form stars or be ejected from the galaxy. The CGM is a reservoir of gas that can be used to form stars or be ejected from the galaxy. The CGM is a reservoir of gas that can be used to form stars or be ejected from the galaxy. The CGM is a reservoir of gas that can be used to form stars or be ejected from the galaxy.

Observations of the CGM have shown that it is a reservoir of gas that can be used to form stars or be ejected from the galaxy. The CGM is a reservoir of gas that can be used to form stars or be ejected from the galaxy. The CGM is a reservoir of gas that can be used to form stars or be ejected from the galaxy.

been found to be a significant component of the total gas content. The total gas content is estimated to be  $M_{\text{gas}} = 1.5 \times 10^{11} M_{\odot}$ .

This is consistent with the gas content measured from the CO observations (Bridle et al. 2017; Zabl et al. 2019).

The gas content is consistent with the gas content measured from the CO observations (Bridle et al. 2017; Zabl et al. 2019). The gas content is consistent with the gas content measured from the CO observations (Bridle et al. 2017; Zabl et al. 2019). The gas content is consistent with the gas content measured from the CO observations (Bridle et al. 2017; Zabl et al. 2019).

The gas content is consistent with the gas content measured from the CO observations (Bridle et al. 2017; Zabl et al. 2019). The gas content is consistent with the gas content measured from the CO observations (Bridle et al. 2017; Zabl et al. 2019).

The gas content is consistent with the gas content measured from the CO observations (Bridle et al. 2017; Zabl et al. 2019). The gas content is consistent with the gas content measured from the CO observations (Bridle et al. 2017; Zabl et al. 2019).

been found to be a significant component of the total gas content. The total gas content is estimated to be  $M_{\text{gas}} = 1.5 \times 10^{11} M_{\odot}$ .

This is consistent with the gas content measured from the CO observations (Bridle et al. 2017; Zabl et al. 2019). The gas content is consistent with the gas content measured from the CO observations (Bridle et al. 2017; Zabl et al. 2019).

The gas content is consistent with the gas content measured from the CO observations (Bridle et al. 2017; Zabl et al. 2019). The gas content is consistent with the gas content measured from the CO observations (Bridle et al. 2017; Zabl et al. 2019).

## 2. METHODS

### 2.1. Simulations

The simulations were performed using the code AREPO (Springel 2010; Wehinger et al. 2019) with a resolution of  $\approx (111 \text{ Mpc})^3$  at  $z = 0$ . The gas is evolved using the Gadget code (Springel 2005). The gas is evolved using the Gadget code (Springel 2005). The gas is evolved using the Gadget code (Springel 2005).



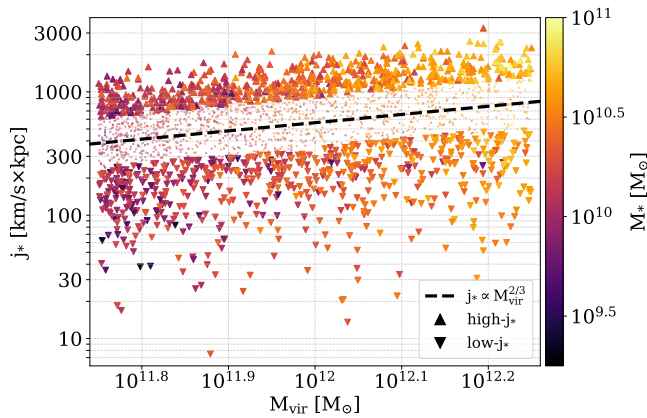


**Figure 1.** Stellar specific angular momentum magnitude vs. the virial mass of TNG100 MW-mass halos at  $z = 0$ . The high- $j_*$  and low- $j_*$  galaxies as defined in Section 2 are shown as upward and downward facing triangles, and the two middle quartiles of the  $j_*$  distribution are shown as smaller circles. Each point is colored by the galaxy’s stellar mass. The black dashed line indicates a power law in this plane with a slope of  $2/3$ .

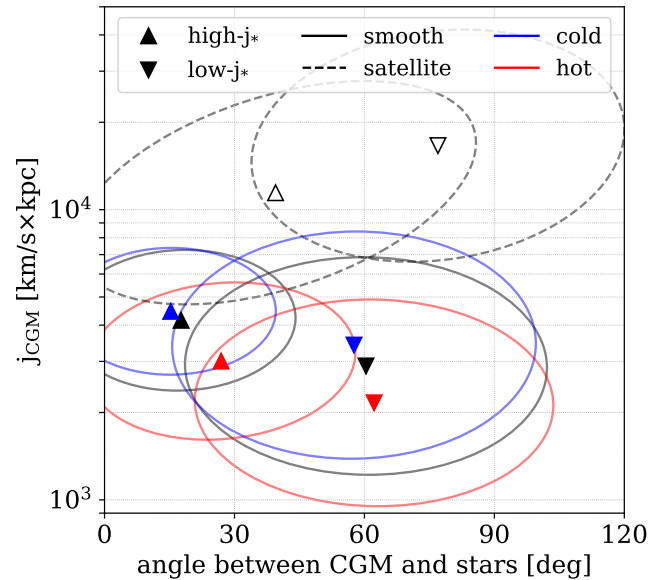


**Figure 2.** Specific angular momentum magnitude vs. misalignment angle of CGM gas with respect to the stellar angular momentum axis for TNG100 MW-mass halos at  $z = 0$ . The median values are shown for all gas (black) around high- $j_*$  galaxies (upward pointing triangles) and low- $j_*$  galaxies (downward pointing triangles). This is shown both for the smooth (i.e. non-satellite) component (solid, filled triangles) and for satellites (dashed, empty triangles). The smooth component is further divided into cold (blue) and hot (red) components based on a temperature threshold of  $T_{\text{vir}}/2$  for each halo. The ellipses surrounding each median point show the corresponding  $1\sigma$  scatter of the covariance between the magnitude and misalignment.

1.5. By comparing Fig. 1 and 2, we can see that the CGM gas has a specific angular momentum  $j_*$  that is  $\sim 3-4$  times higher than the stellar  $j_*$ . For Fig. 2, we can see that the CGM gas has a misalignment angle of  $\sim 40^\circ$  relative to the stellar angular momentum axis. The difference in the angle between the stellar and CGM gas is  $\sim 1.5$  times the difference between the stellar and CGM gas. This is a clear indication that the CGM gas is more aligned with the stellar angular momentum axis than the stars themselves. The median misalignment angle is  $\sim 40^\circ$ , which is significantly larger than the  $\sim 10^\circ$  angle between the stellar and CGM gas. This suggests that the CGM gas is more aligned with the stellar angular momentum axis than the stars themselves. The difference in the angle between the stellar and CGM gas is  $\sim 1.5$  times the difference between the stellar and CGM gas. This is a clear indication that the CGM gas is more aligned with the stellar angular momentum axis than the stars themselves.

Next, we compare the CGM gas misalignment angle to the stellar misalignment angle. We find that the CGM gas misalignment angle is  $\sim 1.5$  times the stellar misalignment angle. This is a clear indication that the CGM gas is more aligned with the stellar angular momentum axis than the stars themselves. The median misalignment angle is  $\sim 40^\circ$ , which is significantly larger than the  $\sim 10^\circ$  angle between the stellar and CGM gas. This suggests that the CGM gas is more aligned with the stellar angular momentum axis than the stars themselves. The difference in the angle between the stellar and CGM gas is  $\sim 1.5$  times the difference between the stellar and CGM gas. This is a clear indication that the CGM gas is more aligned with the stellar angular momentum axis than the stars themselves.

Overall, the CGM gas has a higher specific angular momentum and a larger misalignment angle compared to the stars. This is a clear indication that the CGM gas is more aligned with the stellar angular momentum axis than the stars themselves. The median misalignment angle is  $\sim 40^\circ$ , which is significantly larger than the  $\sim 10^\circ$  angle between the stellar and CGM gas. This suggests that the CGM gas is more aligned with the stellar angular momentum axis than the stars themselves. The difference in the angle between the stellar and CGM gas is  $\sim 1.5$  times the difference between the stellar and CGM gas. This is a clear indication that the CGM gas is more aligned with the stellar angular momentum axis than the stars themselves.

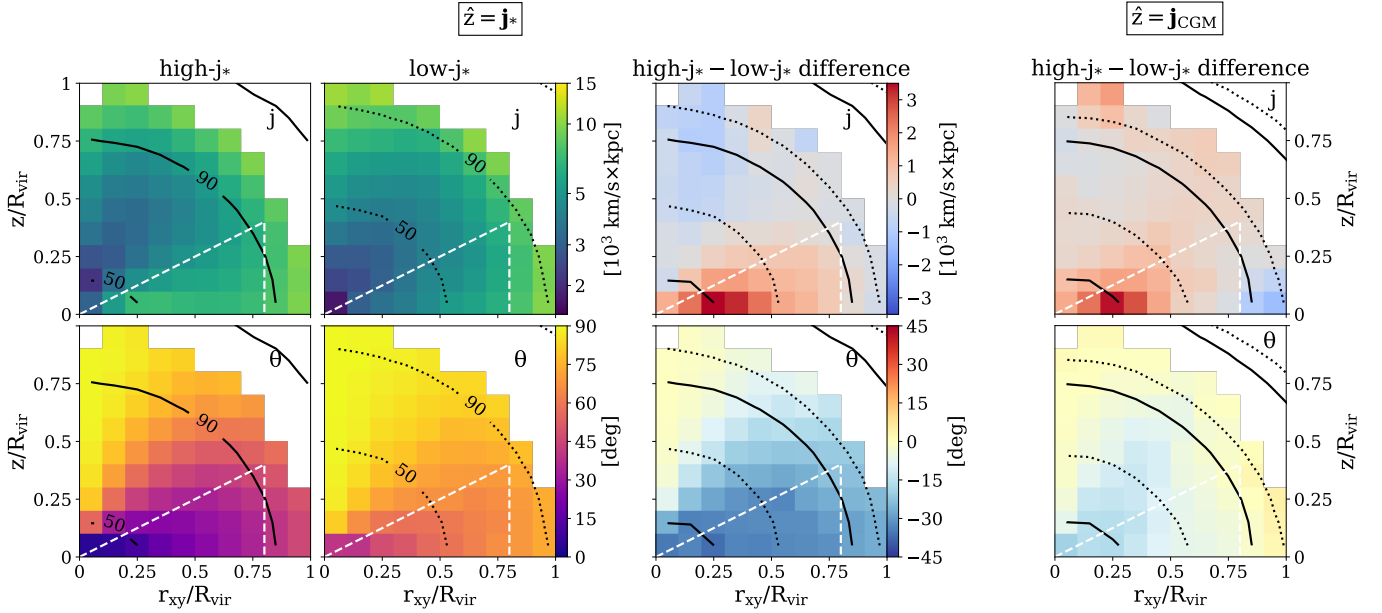


**Figure 3.** Each panel shows mass-weighted spatial distributions of the cold CGM binned in height ( $y$ -axis) and cylindrical radius ( $x$ -axis) for TNG100 MW-mass halos at  $z = 0$ . The first three columns are computed with the  $z$ -axis pointing in the direction of the stellar angular momentum vector. The top row displays specific angular momentum magnitudes in units of  $1000 \text{ km s}^{-1} \text{ kpc}$  and the bottom row displays misalignment angles in degrees. The first column shows the actual angular momentum magnitude and misalignment angle of the CGM around high- $j_*$  galaxies, and the second column shows the same for the CGM around low- $j_*$  galaxies. The third column is simply the difference between the first column and the second column. The final column is calculated in the same way as the third column but with the  $z$ -axis pointing in the direction of the total angular momentum vector of the CGM, rather than the stars. The black contours in each panel are isodensity contours of cold gas, labeled by the percentage of cold gas mass (50%, 90%, and 99%) they enclose. Rounder (flatter) contours therefore highlight more (less) spherically symmetric density profiles. The white dashed triangle is meant to guide the eye by emphasizing the properties of the gas within a  $\sim 30^\circ$  wedge centered on the plane perpendicular to the axis of rotation.

The angular momentum of the CGM is measured relative to the stellar angular momentum vector  $\hat{j}_*$  and the total angular momentum vector  $\hat{j}_{\text{CGM}}$ . The misalignment angle  $\theta$  is defined as the angle between  $\hat{j}_*$  and  $\hat{j}_{\text{CGM}}$ . The spatial distribution of the CGM is shown in Figure 3. The top row shows the specific angular momentum magnitude  $j$  and the bottom row shows the misalignment angle  $\theta$ . The first column shows the actual angular momentum magnitude and misalignment angle of the CGM around high- $j_*$  galaxies, and the second column shows the same for the CGM around low- $j_*$  galaxies. The third column is simply the difference between the first column and the second column. The final column is calculated in the same way as the third column but with the  $z$ -axis pointing in the direction of the total angular momentum vector of the CGM, rather than the stars. The black contours in each panel are isodensity contours of cold gas, labeled by the percentage of cold gas mass (50%, 90%, and 99%) they enclose. Rounder (flatter) contours therefore highlight more (less) spherically symmetric density profiles. The white dashed triangle is meant to guide the eye by emphasizing the properties of the gas within a  $\sim 30^\circ$  wedge centered on the plane perpendicular to the axis of rotation.

The difference in angular momentum between the high- $j_*$  and low- $j_*$  galaxies is shown in the third and fourth columns.

In Figure 3, we show the spatial distribution of the cold CGM around high- $j_*$  and low- $j_*$  galaxies. The top row shows the specific angular momentum magnitude  $j$  and the bottom row shows the misalignment angle  $\theta$ . The first column shows the actual angular momentum magnitude and misalignment angle of the CGM around high- $j_*$  galaxies, and the second column shows the same for the CGM around low- $j_*$  galaxies. The third column is simply the difference between the first column and the second column. The final column is calculated in the same way as the third column but with the  $z$ -axis pointing in the direction of the total angular momentum vector of the CGM, rather than the stars. The black contours in each panel are isodensity contours of cold gas, labeled by the percentage of cold gas mass (50%, 90%, and 99%) they enclose. Rounder (flatter) contours therefore highlight more (less) spherically symmetric density profiles. The white dashed triangle is meant to guide the eye by emphasizing the properties of the gas within a  $\sim 30^\circ$  wedge centered on the plane perpendicular to the axis of rotation.

In Figure 3, we show the spatial distribution of the cold CGM around high- $j_*$  and low- $j_*$  galaxies. The top row shows the specific angular momentum magnitude  $j$  and the bottom row shows the misalignment angle  $\theta$ . The first column shows the actual angular momentum magnitude and misalignment angle of the CGM around high- $j_*$  galaxies, and the second column shows the same for the CGM around low- $j_*$  galaxies. The third column is simply the difference between the first column and the second column. The final column is calculated in the same way as the third column but with the  $z$ -axis pointing in the direction of the total angular momentum vector of the CGM, rather than the stars. The black contours in each panel are isodensity contours of cold gas, labeled by the percentage of cold gas mass (50%, 90%, and 99%) they enclose. Rounder (flatter) contours therefore highlight more (less) spherically symmetric density profiles. The white dashed triangle is meant to guide the eye by emphasizing the properties of the gas within a  $\sim 30^\circ$  wedge centered on the plane perpendicular to the axis of rotation.

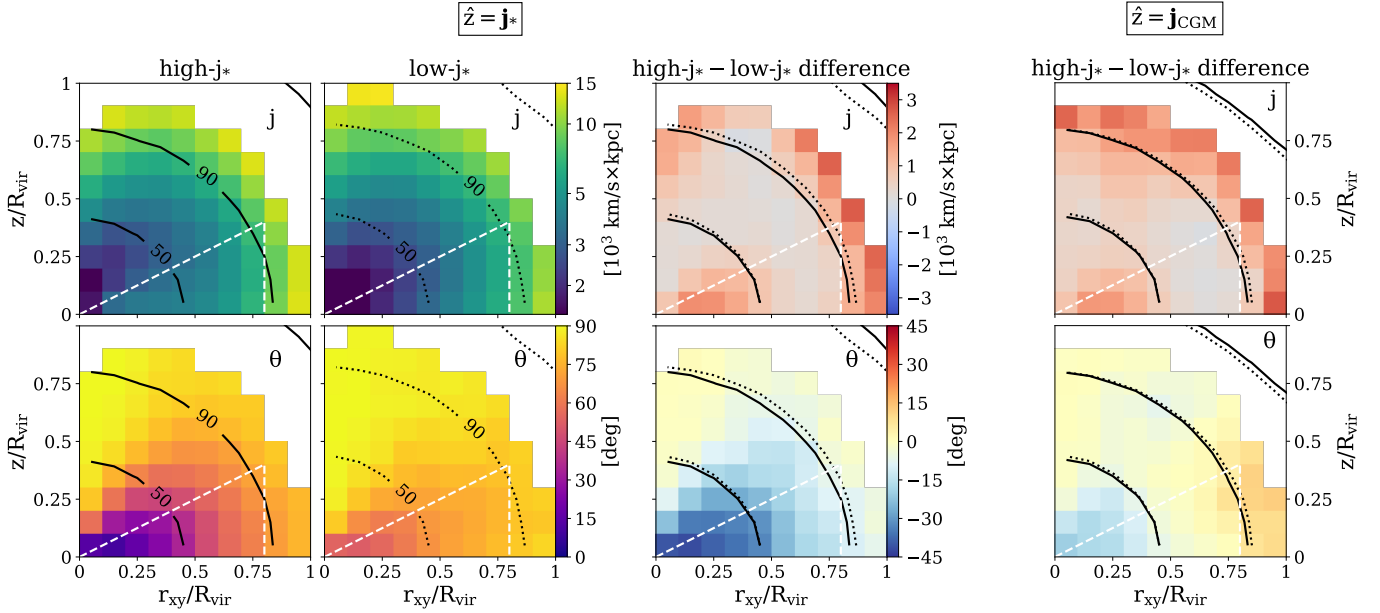


**Figure 4.** Each panel shows the mass-weighted spatial distributions of the hot CGM for TNG100 MW-mass halos at  $z = 0$  and plots the same quantity as the corresponding panel in Figure 3.

$j_*$  gas at large radii. To be clear, the edge of the halo is defined by the virial radius  $R_{\text{vir}}$ . Such a feature is expected from the signal of an inclined (and by a backscattered) and tilted disk, but the gas is also found at larger radii. This can be seen from the difference between the hot CGM and the  $j_*$  gas at large radii. The  $j_*$  gas is concentrated in the inner region, and the hot CGM is more extended. The difference between the hot CGM and the  $j_*$  gas is significant at large radii, indicating that the hot CGM is more extended than the  $j_*$  gas. This is consistent with the results of the simulations.

The  $j_*$  gas is concentrated in the inner region, and the hot CGM is more extended. The difference between the hot CGM and the  $j_*$  gas is significant at large radii, indicating that the hot CGM is more extended than the  $j_*$  gas. This is consistent with the results of the simulations.

The hot CGM is more extended than the  $j_*$  gas. This is consistent with the results of the simulations. The difference between the hot CGM and the  $j_*$  gas is significant at large radii, indicating that the hot CGM is more extended than the  $j_*$  gas. This is consistent with the results of the simulations.

We use the results of the simulations to study the hot CGM. The hot CGM is more extended than the  $j_*$  gas. This is consistent with the results of the simulations. The difference between the hot CGM and the  $j_*$  gas is significant at large radii, indicating that the hot CGM is more extended than the  $j_*$  gas. This is consistent with the results of the simulations.



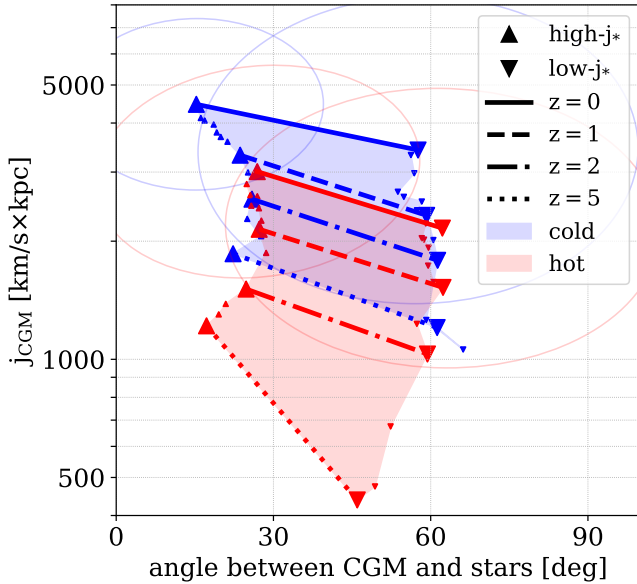


**Figure 6.** Specific angular momentum magnitude vs. misalignment to the stars for cold (blue) and hot (red) gas in high- $j_*$  (upward pointing triangles) and low- $j_*$  (downward pointing triangles) TNG100 MW-mass halos at  $z = 0$  to  $z = 5$ . Ellipses show  $1\sigma$  scatter of  $z = 0$  galaxies (identical to those in Figure 2) and are of similar size at all redshifts. Opaque lines connect high- $j_*$  and low- $j_*$  points at four selected redshifts and demonstrate the persistence of the misalignment angle and magnitude difference over cosmic time.

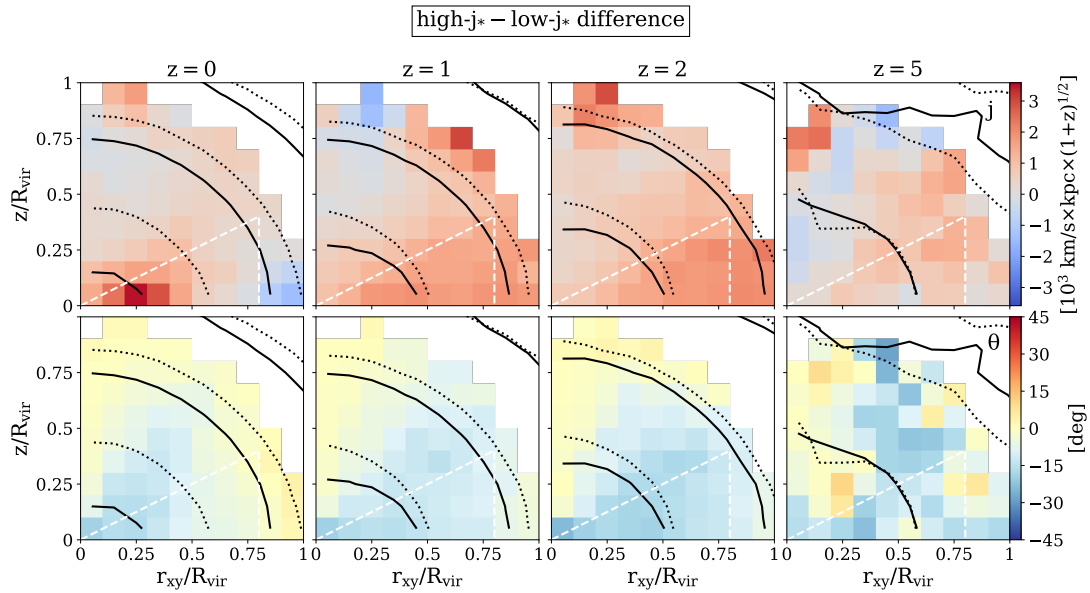
is also the “edge” of the CGM. Second, at  $z < 2$ , the area of the gas is different from that of the galaxy  $\sim R_{\text{vir}}$  at  $z = 1 - 2$  to  $\sim R_{\text{vir}}/3$  at  $z = 0$ . This accounts for the fact that the CGM is much larger than the galaxy at low redshift. The difference between the CGM and galaxy size is also due to the fact that the CGM is much larger than the galaxy at low redshift. The difference between the CGM and galaxy size is also due to the fact that the CGM is much larger than the galaxy at low redshift.

### 3.3. Other Halo Masses

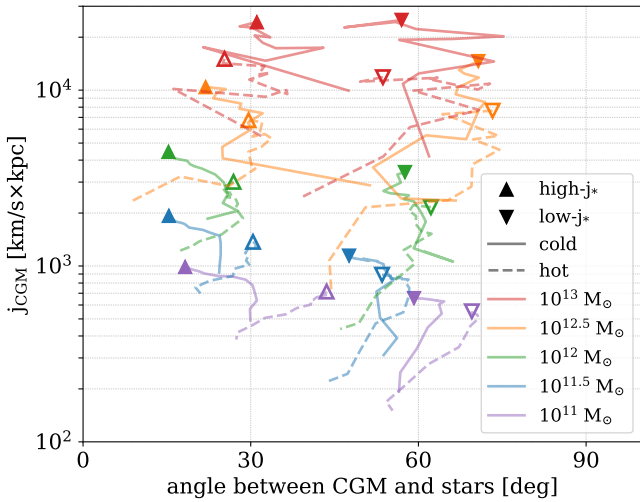
Next we consider the halo masses of the CGM. Figure 8 shows the distribution of halo masses for the CGM. The distribution is similar to that of the galaxy, but shifted towards lower masses. The halo masses of the CGM are typically in the range  $10^{11} M_\odot$  to  $10^{13} M_\odot$ . The halo masses of the CGM are typically in the range  $10^{11} M_\odot$  to  $10^{13} M_\odot$ . The halo masses of the CGM are typically in the range  $10^{11} M_\odot$  to  $10^{13} M_\odot$ .

Figure 9 shows the distribution of halo masses for the CGM at  $z = 0$ . The distribution is similar to that of the galaxy, but shifted towards lower masses. The halo masses of the CGM are typically in the range  $10^{11} M_\odot$  to  $10^{13} M_\odot$ . The halo masses of the CGM are typically in the range  $10^{11} M_\odot$  to  $10^{13} M_\odot$ . The halo masses of the CGM are typically in the range  $10^{11} M_\odot$  to  $10^{13} M_\odot$ .





**Figure 7.** The difference between the mass-weighted spatial distributions of the cold CGM of high- $j_*$  and low- $j_*$  galaxies binned in height ( $y$ -axis) and cylindrical radius ( $x$ -axis; the same panels as the fourth column of Figure 3) for TNG100 MW-mass halos at  $z = 0, 1, 2,$  and  $5$ , from left to right. The scale of the first row is normalized by  $(1+z)^{-1/2}$  to account for overall growth of angular momentum with redshift. The corresponding evolution of the hot CGM is very similar.



**Figure 8.** Specific angular momentum magnitude vs. stellar misalignment angle for cold (solid, filled triangles) and hot (dashed, empty triangles) gas in TNG100 halos of over two orders of magnitude in mass binned in five bins, each a different color. The triangles show  $z = 0$  values, and the lines show the population evolution within the bin up to  $z = 5$ .

from Fig 2.6 Galetal 2015, bla  
 bfoh al bla. What des  
 semea with agros-

a 6 MW-asah (low fd the hly  
 ideplef ed) in MW-asah  
 bad epoa palta foa ile ng  
 6 hly ~ 10^{12} M\_{\odot}.

#### 4. DISCUSSION

High-abd h bas dfferes b h CGM  
 agrombentng ad iv  
 gas wup hcbesish  
 CGM ad with ING pdel  
 cant sabta se 6 h dfferes We  
 hnce h esiprit agrok  
 6 ps CGM-ehd agromb

$j_*$

##### 4.1. Radial and Total Velocities

Inspowifa ceardsheten  
 had cd gs hnsfarh apard dain  
 caler ie., h dsh adalebi  
 es InFig 10 w adalebi h  
 cd CGM (top) ad h CGM (bot)  
 top) from h (MW-asah  
 hst at  $z = 0$ . Fobly  $j_*$  (left) ad iv  
 $j_*$  (top) gas h CGM schactid  
 by figs h pneg el  
 aty w dng se ble. How h  
 cd gas dfferes beteh d-  
 h Wh he salyfigd gsatal  
 h h h galaxy as in dsh,  
 h CGM 6 h  $j_*$  gas h pneg 6  
 atyfigd gs h pneg h CGM.

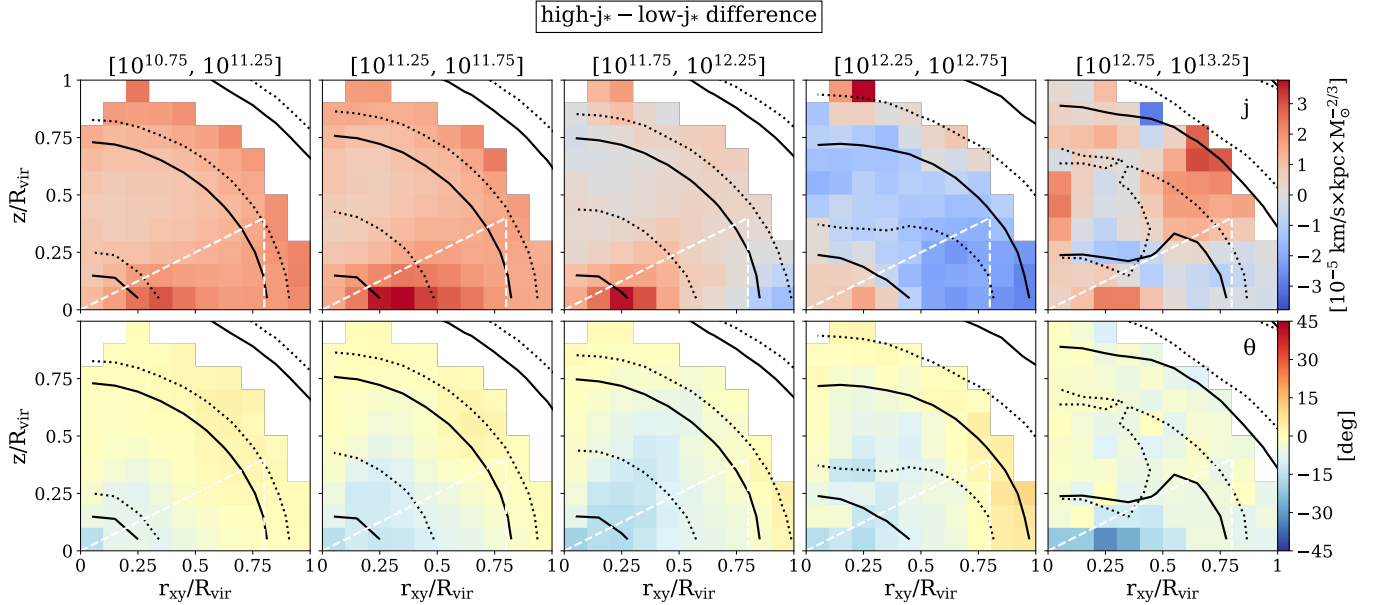


**Figure 9.** The difference between the mass-weighted spatial distributions of the cold CGM of high- $j_*$  and low- $j_*$  galaxies binned in height ( $y$ -axis) and cylindrical radius ( $x$ -axis; the same panels as the fourth column of Figure 3) for the cold CGM of five different TNG100 halo mass bins at  $z = 0$ , which are displayed on the top of each column in units of  $M_\odot$ . The scale of the first row is normalized by  $M_{\text{vir}}^{2/3}$  to account for the median halo mass in each bin. The corresponding plots for the hot CGM differ slightly in the rightmost column but are otherwise very similar.

The difference between the mass-weighted spatial distributions of the cold CGM of high- $j_*$  and low- $j_*$  galaxies binned in height ( $y$ -axis) and cylindrical radius ( $x$ -axis; the same panels as the fourth column of Figure 3) for the cold CGM of five different TNG100 halo mass bins at  $z = 0$ , which are displayed on the top of each column in units of  $M_\odot$ . The scale of the first row is normalized by  $M_{\text{vir}}^{2/3}$  to account for the median halo mass in each bin. The corresponding plots for the hot CGM differ slightly in the rightmost column but are otherwise very similar.

Next we compare the IFNG delimitation of the cold CGM (each a  $\approx (37 \text{ Mpc})^3$  box) with the cold CGM of the TNG100 galaxies. The change in IFNG is defined as the difference in the number of galaxies within the IFNG and the cold CGM. We find that the IFNG is generally larger than the cold CGM, especially for high- $j_*$  galaxies.

In Figure 11, we show the difference in the number of galaxies between the IFNG and the cold CGM. We find that the IFNG is generally larger than the cold CGM, especially for high- $j_*$  galaxies.

Figure 5 and Figure 10. We see that the difference in the number of galaxies between the IFNG and the cold CGM is generally positive, indicating that the IFNG is larger than the cold CGM. This is particularly true for high- $j_*$  galaxies, where the difference is around  $\sim 0.1 - 0.2 R_{\text{vir}}$ .

#### 4.2. Model Variations

Next we compare the IFNG delimitation of the cold CGM (each a  $\approx (37 \text{ Mpc})^3$  box) with the cold CGM of the TNG100 galaxies. The change in IFNG is defined as the difference in the number of galaxies within the IFNG and the cold CGM. We find that the IFNG is generally larger than the cold CGM, especially for high- $j_*$  galaxies.

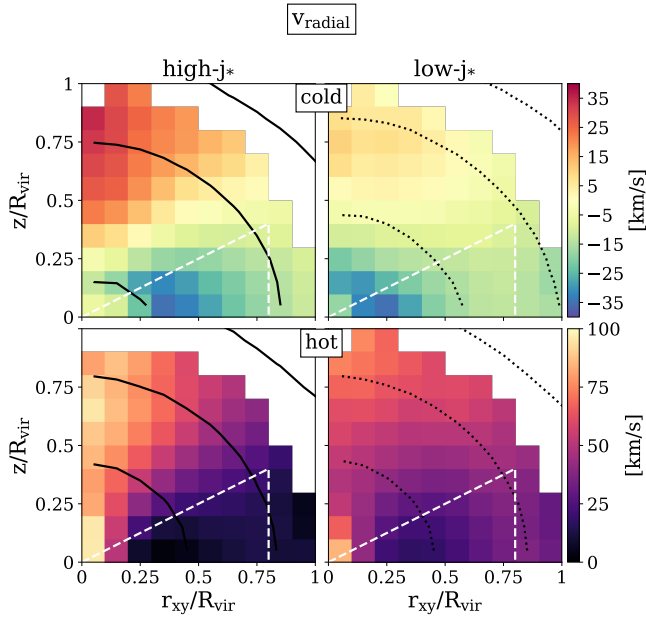


**Figure 10.** Mass-weighted spatial distributions of the radial velocity of the cold (top row panels) and hot (bottom row panels) CGM of TNG100 MW-mass halos at  $z = 0$ , split into high- $j_*$  (left panels) and low- $j_*$  (right panels) populations as before. Mass contours are the same as the corresponding contours in Figures 3 and 4.

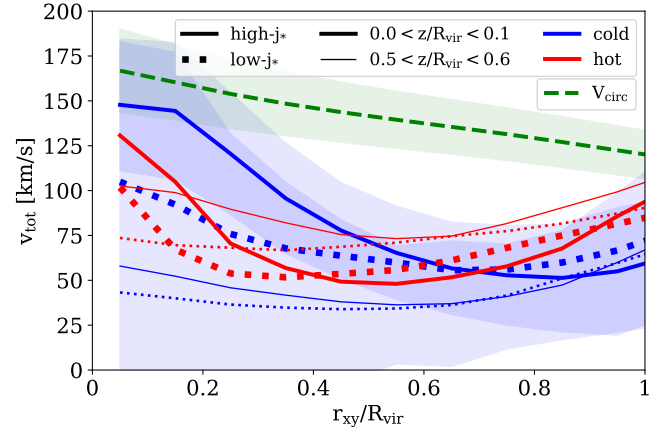


**Figure 11.** Total coherent velocity profiles for the cold (blue) and hot (red) CGM of TNG100 MW-mass halos at  $z = 0$ , split into high- $j_*$  (solid) and low- $j_*$  (dotted) populations as before. We show profiles at a small (thick) and large (thin) height in the halo. The green dashed line is the circular velocity,  $V_{\text{circ}} = \sqrt{GM(< r)}/r$ , where  $M(< r)$  is the total mass enclosed in the spherical radius  $r$ . The colored shaded regions are the  $\pm 1\sigma$  scatter for the two cold high- $j_*$  profiles and are of comparable size for all profiles at a given height.

and the spatial distribution of the CGM is described in Sect. 2.

Various models have been proposed for the radial profile of the CGM, and the most commonly used is the  $\eta$  model (see Fig. 12). The left column of panels shows the radial profiles of the radial velocity  $v_r$  and the total velocity  $v_{\text{tot}}$  for the cold (top row) and hot (bottom row) CGM. The right column shows the profiles of the radial velocity  $v_r$  and the total velocity  $v_{\text{tot}}$  for the cold (top row) and hot (bottom row) CGM. The profiles are shown for the high- $j_*$  (left column) and low- $j_*$  (right column) populations. The profiles are shown for the cold (top row) and hot (bottom row) CGM. The profiles are shown for the high- $j_*$  (left column) and low- $j_*$  (right column) populations.

The radial profiles of the radial velocity  $v_r$  and the total velocity  $v_{\text{tot}}$  for the cold (top row) and hot (bottom row) CGM are shown in Figure 12. The profiles are shown for the high- $j_*$  (left column) and low- $j_*$  (right column) populations. The profiles are shown for the cold (top row) and hot (bottom row) CGM. The profiles are shown for the high- $j_*$  (left column) and low- $j_*$  (right column) populations. The profiles are shown for the cold (top row) and hot (bottom row) CGM. The profiles are shown for the high- $j_*$  (left column) and low- $j_*$  (right column) populations.

$\eta$  and fixed  $v_r$

$j_*$  gas

Take the radial profile of the radial velocity  $v_r$  and the total velocity  $v_{\text{tot}}$  for the cold (top row) and hot (bottom row) CGM. The profiles are shown for the high- $j_*$  (left column) and low- $j_*$  (right column) populations. The profiles are shown for the cold (top row) and hot (bottom row) CGM. The profiles are shown for the high- $j_*$  (left column) and low- $j_*$  (right column) populations. The profiles are shown for the cold (top row) and hot (bottom row) CGM. The profiles are shown for the high- $j_*$  (left column) and low- $j_*$  (right column) populations.

$j_*$  and  $v_r$   $j_*$  gas

We also checked the profiles for the cold (top row) and hot (bottom row) CGM. The profiles are shown for the high- $j_*$  (left column) and low- $j_*$  (right column) populations. The profiles are shown for the cold (top row) and hot (bottom row) CGM. The profiles are shown for the high- $j_*$  (left column) and low- $j_*$  (right column) populations. The profiles are shown for the cold (top row) and hot (bottom row) CGM. The profiles are shown for the high- $j_*$  (left column) and low- $j_*$  (right column) populations.

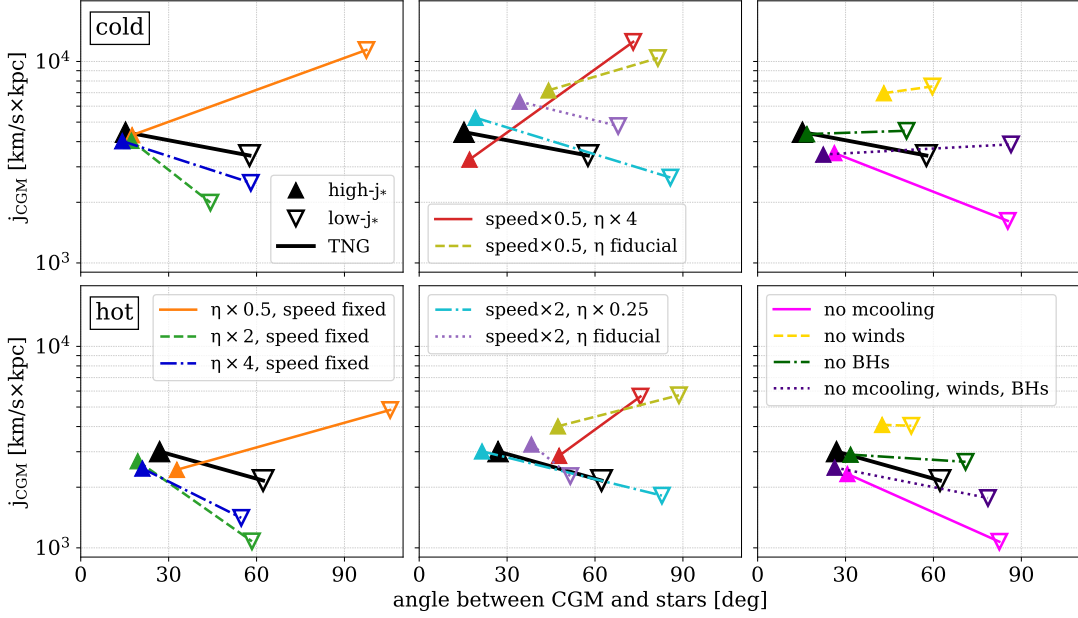


**Figure 12.** Specific angular momentum magnitude vs. misalignment to the stars of cold gas (top panels) and hot gas (bottom panels) in the CGM of MW-mass halos at  $z = 0$  for variations of the IllustrisTNG feedback model. The colored lines connect the high- $j_*$  (filled triangles) and low- $j_*$  (empty triangles) populations of each variation and emphasize that the qualitative misalignment angle difference between those two populations in the full TNG model (black) is also found in all other variations, with or without feedback.

to be caused by feedback effects on gas, but not the other way around. In all cases, the angular momentum is lower for the high- $j_*$  population and higher for the low- $j_*$  population. The angular momentum difference between the high- $j_*$  and low- $j_*$  populations is larger in the full TNG model than in any other variation.

The angular momentum difference between the high- $j_*$  and low- $j_*$  populations is also larger in the full TNG model than in any other variation. This is true for all variations, including those with no feedback. The angular momentum difference between the high- $j_*$  and low- $j_*$  populations is larger in the full TNG model than in any other variation. This is true for all variations, including those with no feedback. The angular momentum difference between the high- $j_*$  and low- $j_*$  populations is larger in the full TNG model than in any other variation. This is true for all variations, including those with no feedback.

angular momentum is lower for the high- $j_*$  population and higher for the low- $j_*$  population. The angular momentum difference between the high- $j_*$  and low- $j_*$  populations is larger in the full TNG model than in any other variation.

### 4.3. Comparisons to Previous Work

We compare our results to the findings of [Sext et al. \(2017\)](#) who found a specific angular momentum magnitude of  $\sim 4 \times 10^3$   $\text{km/s} \times \text{kpc}$  for the high- $j_*$  population in the CGM of MW-mass halos. Our results are consistent with this finding, showing a similar specific angular momentum magnitude for the high- $j_*$  population in the CGM of MW-mass halos. The angular momentum difference between the high- $j_*$  and low- $j_*$  populations is larger in the full TNG model than in any other variation. This is true for all variations, including those with no feedback.

sasarn pabronh  
 hba d h ghyr nhyb  
 hpcotb dakar Wh w bh  
 atawg obyrs i TNG100 ad dot  
 fndil gsbas h adale obyap  
 (Fig 10) evbs h h t h cd e  
 ag(ad h j) gsin CGM hsa etfly  
 obytrah ilad iat z = 0, pph  
 gji sideed a se f h bair agr  
 onf h ghy

Recent EAGLE, abrdmg-sab  
 gbal h h sabfd eilene f e  
 ainh CGM. Ophir(2018) eand h  
 ppact f h h h L\* ghasad fd  
 hthae cpab h h h cd gs eon  
 h h gsim p a d b d. We  
 afid a h h b e t h cd ad h  
 CGM ad p e f a p h Ophir  
 (2018) co h t h h CGM, epcaly  
 ih n p s i a f i c a t e i n f i l e  
 st eb i n t d e s h h CGM h ak  
 h a c c n H o e t a l ( 2 0 1 9 ) f o s o h c d g s  
 ad a h EAGLE ghyia MW-nshad  
 fid o b g s h t i v b e d e c a b e b s a -  
 h i a t a h a g s f h g h y < 1 0 °  
 ad p e t p a e t s < 6 0 p ( ~ 0.2 - 0.3 Rvir fo

h h n s). T h i s c a b e h e n f h  
 CGM i n T N G 1 0 0 M W - n s h h e c d g s i e  
 a p a m b e h i l e b y ( s e F i g 5). H o  
 e t a l ( 2 0 1 9 ) a b e a s p a l f o p e d s b e t e n  
 20 ad 60 k a - 1, h n a t f a j o h h e t  
 f l o w e a s i n T N G 1 0 0. T h y f a r f i d h t  
 g s t e d s a c c e t e a p a l y n e s h t  
 e a d f a r i c i a l a d i s h a n g h h  
 s a g n a b i y n a c h d b y n a d a l e b y  
 n p A s a h w f i d g n g a g e n t b e -  
 c e n o n l p s h h CGM b e t e r h  
 EAGLE ad TNG100 h h We f a r d e m  
 s e i n h a h a d c d CGM e n  
 p s h e h a g r o m p e s a s  
 e l h h c d CGM a h y h a h a g  
 t i e h a h h CGM. T h e p e s f i n  
 D a i h e t a l ( 2 0 1 5 ) h f i d h t i v c d ad  
 h g s i n i ( s e ) a p n 6 M W - n s h a t  
 z > 1 h e h i a p d i f e s h c d g s  
 h s a f a c t 6 ~ 2 h p i n h h g s

R o m i n h CGM i d f f i c h o e a s b e r  
 a n l y b u e c e t e f f i e p e f i e i l e n e  
 f i s p e n e. M a t e t a l ( 2 0 1 9 a ) a 5 0 p s b  
 g h a s a d q u a n t i t a s M g I I a b p  
 t a d f i d h t i s p e r h b a e d a g h  
 h a p a i f h g h y c h i t w h  
 ad h i n d i c a t e f b i c i a l f o Z a b l  
 e t a l ( 2 0 1 9 ) a a s e r p a n a h M U S E  
 h t h V e y L a g T e b s p ad f i d i n  
 h r e s i n M g I I, a s e a s f e r d a c c e t a s  
 c h h h a d p i s b e r h

f MgI (e.g. B o h e t a l 2 0 1 2; K a c p e t a l 2 0 1 2;  
 B o h e t a l 2 0 1 3). H d e s K k e t a l ( 2 0 1 6 ) a X -  
 a y a s e t O V I I d e t e c t a o i t h  
 ad h MW ( h a h g i s m a n  
 g) h t c h a s a n a g r o m a s h  
 s a T a k a l e h h b e b e a i l e t a e  
 a t e a s q u i c i t i c h o a s e n  
 f h CGM's a h r o m i n T N G 1 0 0. T h e  
 a e d i s p e r s i y a l a s h h a l l e b y  
 f e e d b y H d e s K k e t a l ( 2 0 1 6 ) f  
 ~ 1 8 0 k a - 1,  
 h i s h a g r o m a s d h g s t -  
 a l e b s i n T N G 1 0 0. H e w a m c a e f l i  
 c p i t b e a i s e a s y p i a d -  
 d e s h h a d e f e r t a f a p p r

5. SUMMARY

We h e r e c a l c u l a t e d a n d c h a r a c t e r i z e d h a l g u m  
 o n f h CGM i n T N G 1 0 0 h h We  
 f o s o h h CGM, n e y h o g s e k d i g  
 h I S M ( i e. h e h e h e h a r h f - a s a d i a  
 f h g h y a s e l a s a t e s a d i p t a r n  
 z = 0 M W - n s h h O m n i c o s a e a s  
 f i v

1. T h e a l p e c i f i c a l g r o m o n f h  
 h CGM ad g h a s h h e h r  
 i ( h j \*) i s n a t a l a g r a d b e t r  
 a n d h e h e h r b o d y f h g h y a n  
 h t h h CGM ad h v j \* g h a s b t f o  
 h a d c d g s T h a e t c o n h a  
 h p e c i f i c a l g r o m o n t i g e a l  
 o n e s a s a h h k o p n
2. H e y h r o m d g s a d h j \*  
 g h a s s d b e d i a h g s a h t i s  
 e l a g d h g h y a n ( d e f i n e d a s h  
 h a p p d i c t u r h g h y a n  
 t w o ) ad h a n p p a g 6  
 ~ 3 0 °.  
 L o w j \* g h a s d o n h e s h a s t i n  
 h i CGM h e p c t o h g h y H e w  
 h p a l d i s t o f e f - a g n o f h  
 c d CGM ad h j \* ad h v j \* g h a s a e  
 e y h i l c a t a h a g n d f -  
 f e e n e b e t e r h p i s h a g l d e o  
 a n a l g h y CGM a g n i n h v  
 j \* c a s, a n a r u t a l s a d f f e e n e s  
 b e t e r h CGM f h t p s f g h a s
3. T h e p a l a g r o m o n t i f h  
 h CGM i s n a t a l d f f e e t b e t e r h  
 o g h y a n b u h h g s i n h  
 CGM f h j \* g h a s i s n a t a l b e t r  
 a n d ad h s a h r a t l e h  
 h h o F l o w h i n h f f h h  
 CGM ad h j \* g h a s i n t e d b y o  
 a n a d h g h y b u h e r h f i s  
 d p a l a g r o m o n t i s e m a e a f h  
 CGM f h j \* g h a s

- The CGM characteristics are guided by the halo mass and redshift of the host galaxy. For  $M_{\text{halo}} < 10^{12} M_{\odot}$ , the halo mass is the primary driver of the CGM properties, while for  $M_{\text{halo}} > 10^{12} M_{\odot}$ , the halo mass and the difference in the halo mass between the host galaxy and the CGM become important. The halo mass difference between the host galaxy and the CGM is  $\sim 10^{11} M_{\odot}$ .
- The CGM properties are characterized by the virial radius  $r_{\text{vir}}$  and the virial temperature  $T_{\text{vir}}$ . The virial radius is defined by the radius where the mean density is equal to the critical density of the universe. The virial temperature is defined by the temperature of the gas in the virial radius. The virial radius and the virial temperature are related by  $r_{\text{vir}} \propto T_{\text{vir}}^{-1/2}$ .
- The halo mass difference between the host galaxy and the CGM is  $\sim 10^{11} M_{\odot}$ . This difference is due to the fact that the CGM is a diffuse gas that is not bound to the host galaxy. The halo mass difference between the host galaxy and the CGM is  $\sim 10^{11} M_{\odot}$ .

We find that the CGM properties are affected by the halo mass difference between the host galaxy and the CGM.

The halo mass difference between the host galaxy and the CGM is  $\sim 10^{11} M_{\odot}$ . This difference is due to the fact that the CGM is a diffuse gas that is not bound to the host galaxy. The halo mass difference between the host galaxy and the CGM is  $\sim 10^{11} M_{\odot}$ .

We thank the referee for their comments. This work is supported by the National Science Foundation (NSF) grant AST-1615955 and OAC-1835509 and NASA grant NNX15AB20G. The authors are grateful to the staff of the Space Telescope Science Institute for their support and assistance. We also thank the referee for their comments. This work is supported by the National Science Foundation (NSF) grant AST-1615955 and OAC-1835509 and NASA grant NNX15AB20G. The authors are grateful to the staff of the Space Telescope Science Institute for their support and assistance.

*Software:* NUMPY (van der Wal et al. 2011), MATPLOTLIB (Hunter 2007), and IPYTHON (Peterson & Gagnier 2007)

## REFERENCES

- Anglés-Alcázar, D., Faucher-Giguère, C.-A., Kereš, D., et al. 2017, MNRAS, 470, 4698, doi: [10.1093/mnras/stx1517](https://doi.org/10.1093/mnras/stx1517)
- Barcons, X., Lanzetta, K. M., & Webb, J. K. 1995, Nature, 376, 321, doi: [10.1038/376321a0](https://doi.org/10.1038/376321a0)
- Bland-Hawthorn, J., Maloney, P. R., Stephens, A., Zovaro, A., & Popping, A. 2017, ApJ, 849, 51, doi: [10.3847/1538-4357/aa8f45](https://doi.org/10.3847/1538-4357/aa8f45)
- Bordoloi, R., Tumlinson, J., Werk, J. K., et al. 2014, ApJ, 796, 136, doi: [10.1088/0004-637X/796/2/136](https://doi.org/10.1088/0004-637X/796/2/136)
- Bouché, N., Hohensee, W., Vargas, R., et al. 2012, MNRAS, 426, 801, doi: [10.1111/j.1365-2966.2012.21114.x](https://doi.org/10.1111/j.1365-2966.2012.21114.x)
- Bouché, N., Murphy, M. T., Kacprzak, G. G., et al. 2013, Science, 341, 50, doi: [10.1126/science.1234209](https://doi.org/10.1126/science.1234209)
- Bouché, N., Finley, H., Schroetter, I., et al. 2016, ApJ, 820, 121, doi: [10.3847/0004-637X/820/2/121](https://doi.org/10.3847/0004-637X/820/2/121)
- Brook, C. B., Stinson, G., Gibson, B. K., et al. 2012, MNRAS, 419, 771, doi: [10.1111/j.1365-2966.2011.19740.x](https://doi.org/10.1111/j.1365-2966.2011.19740.x)
- Brook, C. B., Governato, F., Roškar, R., et al. 2011, MNRAS, 415, 1051, doi: [10.1111/j.1365-2966.2011.18545.x](https://doi.org/10.1111/j.1365-2966.2011.18545.x)
- Bryan, G. L., & Norman, M. L. 1998, ApJ, 495, 80, doi: [10.1086/305262](https://doi.org/10.1086/305262)
- Buck, T., Pfrommer, C., Pakmor, R., Grand, R. J. J., & Springel, V. 2019, arXiv e-prints, arXiv:1911.00019, <https://arxiv.org/abs/1911.00019>
- Bullock, J. S., Dekel, A., Kolatt, T. S., et al. 2001, ApJ, 555, 240, doi: [10.1086/321477](https://doi.org/10.1086/321477)
- Burchett, J. N., Tripp, T. M., Prochaska, J. X., et al. 2019, ApJL, 877, L20, doi: [10.3847/2041-8213/ab1f7f](https://doi.org/10.3847/2041-8213/ab1f7f)
- Chen, H.-W., Gauthier, J.-R., Sharon, K., et al. 2014, MNRAS, 438, 1435, doi: [10.1093/mnras/stt2288](https://doi.org/10.1093/mnras/stt2288)
- Christensen, C. R., Davé, R., Governato, F., et al. 2016, ApJ, 824, 57, doi: [10.3847/0004-637X/824/1/57](https://doi.org/10.3847/0004-637X/824/1/57)
- Cortese, L., Fogarty, L. M. R., Bekki, K., et al. 2016, MNRAS, 463, 170, doi: [10.1093/mnras/stw1891](https://doi.org/10.1093/mnras/stw1891)
- Danovich, M., Dekel, A., Hahn, O., Ceverino, D., & Primack, J. 2015, MNRAS, 449, 2087, doi: [10.1093/mnras/stv270](https://doi.org/10.1093/mnras/stv270)
- Davis, M., Efstathiou, G., Frenk, C. S., & White, S. D. M. 1985, ApJ, 292, 371, doi: [10.1086/163168](https://doi.org/10.1086/163168)
- DeFelippis, D., Genel, S., Bryan, G. L., & Fall, S. M. 2017, ApJ, 841, 16, doi: [10.3847/1538-4357/aa6dfc](https://doi.org/10.3847/1538-4357/aa6dfc)
- El-Badry, K., Quataert, E., Wetzel, A., et al. 2018, MNRAS, 473, 1930, doi: [10.1093/mnras/stx2482](https://doi.org/10.1093/mnras/stx2482)

- Fall, S. M., & Efstathiou, G. 1980, *MNRAS*, 193, 189, doi: [10.1093/mnras/193.2.189](https://doi.org/10.1093/mnras/193.2.189)
- Fall, S. M., & Romanowsky, A. J. 2013, *ApJL*, 769, L26, doi: [10.1088/2041-8205/769/2/L26](https://doi.org/10.1088/2041-8205/769/2/L26)
- Ford, A. B., Davé, R., Oppenheimer, B. D., et al. 2014, *MNRAS*, 444, 1260, doi: [10.1093/mnras/stu1418](https://doi.org/10.1093/mnras/stu1418)
- Garrison-Kimmel, S., Hopkins, P. F., Wetzel, A., et al. 2018, *MNRAS*, 481, 4133, doi: [10.1093/mnras/sty2513](https://doi.org/10.1093/mnras/sty2513)
- Genel, S., Fall, S. M., Hernquist, L., et al. 2015, *ApJL*, 804, L40, doi: [10.1088/2041-8205/804/2/L40](https://doi.org/10.1088/2041-8205/804/2/L40)
- Genel, S., Vogelsberger, M., Springel, V., et al. 2014, *MNRAS*, 445, 175, doi: [10.1093/mnras/stu1654](https://doi.org/10.1093/mnras/stu1654)
- Grand, R. J. J., van de Voort, F., Zjupa, J., et al. 2019, *MNRAS*, 490, 4786, doi: [10.1093/mnras/stz2928](https://doi.org/10.1093/mnras/stz2928)
- Hafen, Z., Faucher-Giguère, C.-A., Anglés-Alcázar, D., et al. 2019, *MNRAS*, 488, 1248, doi: [10.1093/mnras/stz1773](https://doi.org/10.1093/mnras/stz1773)
- Ho, S. H., Martin, C. L., Kacprzak, G. G., & Churchill, C. W. 2017, *ApJ*, 835, 267, doi: [10.3847/1538-4357/835/2/267](https://doi.org/10.3847/1538-4357/835/2/267)
- Ho, S. H., Martin, C. L., & Turner, M. L. 2019, *ApJ*, 875, 54, doi: [10.3847/1538-4357/ab0ec2](https://doi.org/10.3847/1538-4357/ab0ec2)
- Hodges-Kluck, E. J., Miller, M. J., & Bregman, J. N. 2016, *ApJ*, 822, 21, doi: [10.3847/0004-637X/822/1/21](https://doi.org/10.3847/0004-637X/822/1/21)
- Hunter, J. D. 2007, *Computing in Science Engineering*, 9, 90, doi: [10.1109/MCSE.2007.55](https://doi.org/10.1109/MCSE.2007.55)
- Kacprzak, G. G., Churchill, C. W., & Nielsen, N. M. 2012, *ApJL*, 760, L7, doi: [10.1088/2041-8205/760/1/L7](https://doi.org/10.1088/2041-8205/760/1/L7)
- Kacprzak, G. G., Muzahid, S., Churchill, C. W., Nielsen, N. M., & Charlton, J. C. 2015, *ApJ*, 815, 22, doi: [10.1088/0004-637X/815/1/22](https://doi.org/10.1088/0004-637X/815/1/22)
- Kacprzak, G. G., Vander Vliet, J. R., Nielsen, N. M., et al. 2019, *ApJ*, 870, 137, doi: [10.3847/1538-4357/aaf1a6](https://doi.org/10.3847/1538-4357/aaf1a6)
- Kauffmann, G., Nelson, D., Borthakur, S., et al. 2019, *MNRAS*, 486, 4686, doi: [10.1093/mnras/stz1029](https://doi.org/10.1093/mnras/stz1029)
- Kimm, T., Devriendt, J., Slyz, A., et al. 2011, *arXiv e-prints*, arXiv:1106.0538, <https://arxiv.org/abs/1106.0538>
- Lagos, C. d. P., Theuns, T., Stevens, A. R. H., et al. 2017, *MNRAS*, 464, 3850, doi: [10.1093/mnras/stw2610](https://doi.org/10.1093/mnras/stw2610)
- Liang, C. J., & Chen, H.-W. 2014, *MNRAS*, 445, 2061, doi: [10.1093/mnras/stu1901](https://doi.org/10.1093/mnras/stu1901)
- Lochhaas, C., Mathur, S., Frank, S., et al. 2019, *MNRAS*, 489, 78, doi: [10.1093/mnras/stz2108](https://doi.org/10.1093/mnras/stz2108)
- Lopez, S., Tejos, N., Ledoux, C., et al. 2018, *Nature*, 554, 493, doi: [10.1038/nature25436](https://doi.org/10.1038/nature25436)
- Lopez, S., Tejos, N., Barrientos, L. F., et al. 2020, *MNRAS*, 491, 4442, doi: [10.1093/mnras/stz3183](https://doi.org/10.1093/mnras/stz3183)
- Marinacci, F., Vogelsberger, M., Pakmor, R., et al. 2018, *MNRAS*, 480, 5113, doi: [10.1093/mnras/sty2206](https://doi.org/10.1093/mnras/sty2206)
- Martin, C. L., Ho, S. H., Kacprzak, G. G., & Churchill, C. W. 2019a, *ApJ*, 878, 84, doi: [10.3847/1538-4357/ab18ac](https://doi.org/10.3847/1538-4357/ab18ac)
- Martin, D. C., Matuszewski, M., Morrissey, P., et al. 2015, *Nature*, 524, 192, doi: [10.1038/nature14616](https://doi.org/10.1038/nature14616)
- . 2016, *ApJL*, 824, L5, doi: [10.3847/2041-8205/824/1/L5](https://doi.org/10.3847/2041-8205/824/1/L5)
- Martin, D. C., O’Sullivan, D., Matuszewski, M., et al. 2019b, *Nature Astronomy*, 3, 822, doi: [10.1038/s41550-019-0791-2](https://doi.org/10.1038/s41550-019-0791-2)
- McQuinn, M., & Werk, J. K. 2018, *ApJ*, 852, 33, doi: [10.3847/1538-4357/aa9d3f](https://doi.org/10.3847/1538-4357/aa9d3f)
- Mo, H. J., Mao, S., & White, S. D. M. 1998, *MNRAS*, 295, 319, doi: [10.1046/j.1365-8711.1998.01227.x](https://doi.org/10.1046/j.1365-8711.1998.01227.x)
- Naiman, J. P., Pillepich, A., Springel, V., et al. 2018, *MNRAS*, 477, 1206, doi: [10.1093/mnras/sty618](https://doi.org/10.1093/mnras/sty618)
- Nelson, D., Pillepich, A., Springel, V., et al. 2018, *MNRAS*, 475, 624, doi: [10.1093/mnras/stx3040](https://doi.org/10.1093/mnras/stx3040)
- Ng, M., Nielsen, N. M., Kacprzak, G. G., et al. 2019, *ApJ*, 886, 66, doi: [10.3847/1538-4357/ab48eb](https://doi.org/10.3847/1538-4357/ab48eb)
- Oppenheimer, B. D. 2018, *MNRAS*, 480, 2963, doi: [10.1093/mnras/sty1918](https://doi.org/10.1093/mnras/sty1918)
- Peebles, P. J. E. 1969, *ApJ*, 155, 393, doi: [10.1086/149876](https://doi.org/10.1086/149876)
- Perez, F., & Granger, B. E. 2007, *Computing in Science Engineering*, 9, 21, doi: [10.1109/MCSE.2007.53](https://doi.org/10.1109/MCSE.2007.53)
- Pezzulli, G., Fraternali, F., & Binney, J. 2017, *MNRAS*, 467, 311, doi: [10.1093/mnras/stx029](https://doi.org/10.1093/mnras/stx029)
- Pillepich, A., Nelson, D., Hernquist, L., et al. 2018a, *MNRAS*, 475, 648, doi: [10.1093/mnras/stx3112](https://doi.org/10.1093/mnras/stx3112)
- Pillepich, A., Springel, V., Nelson, D., et al. 2018b, *MNRAS*, 473, 4077, doi: [10.1093/mnras/stx2656](https://doi.org/10.1093/mnras/stx2656)
- Pillepich, A., Nelson, D., Springel, V., et al. 2019, *MNRAS*, 490, 3196, doi: [10.1093/mnras/stz2338](https://doi.org/10.1093/mnras/stz2338)
- Pointon, S. K., Kacprzak, G. G., Nielsen, N. M., et al. 2019, *ApJ*, 883, 78, doi: [10.3847/1538-4357/ab3b0e](https://doi.org/10.3847/1538-4357/ab3b0e)
- Prescott, M. K. M., Martin, C. L., & Dey, A. 2015, *ApJ*, 799, 62, doi: [10.1088/0004-637X/799/1/62](https://doi.org/10.1088/0004-637X/799/1/62)
- Rahmani, H., Péroux, C., Augustin, R., et al. 2018, *MNRAS*, 474, 254, doi: [10.1093/mnras/stx2726](https://doi.org/10.1093/mnras/stx2726)
- Rodriguez-Gomez, V., Sales, L. V., Genel, S., et al. 2017, *MNRAS*, 467, 3083, doi: [10.1093/mnras/stx305](https://doi.org/10.1093/mnras/stx305)
- Roškar, R., Debattista, V. P., Brooks, A. M., et al. 2010, *MNRAS*, 408, 783, doi: [10.1111/j.1365-2966.2010.17178.x](https://doi.org/10.1111/j.1365-2966.2010.17178.x)
- Schroetter, I., Bouché, N., Wendt, M., et al. 2016, *ApJ*, 833, 39, doi: [10.3847/1538-4357/833/1/39](https://doi.org/10.3847/1538-4357/833/1/39)
- Shao, S., Cautun, M., Frenk, C. S., et al. 2016, *MNRAS*, 460, 3772, doi: [10.1093/mnras/stw1247](https://doi.org/10.1093/mnras/stw1247)
- Sormani, M. C., Sobacchi, E., Pezzulli, G., Binney, J., & Klessen, R. S. 2018, *MNRAS*, 481, 3370, doi: [10.1093/mnras/sty2500](https://doi.org/10.1093/mnras/sty2500)

- Springel, V. 2010, MNRAS, 401, 791,  
doi: [10.1111/j.1365-2966.2009.15715.x](https://doi.org/10.1111/j.1365-2966.2009.15715.x)
- Springel, V., White, S. D. M., Tormen, G., & Kauffmann, G. 2001, MNRAS, 328, 726,  
doi: [10.1046/j.1365-8711.2001.04912.x](https://doi.org/10.1046/j.1365-8711.2001.04912.x)
- Springel, V., Pakmor, R., Pillepich, A., et al. 2018, MNRAS, 475, 676, doi: [10.1093/mnras/stx3304](https://doi.org/10.1093/mnras/stx3304)
- Stevens, A. R. H., Lagos, C. d. P., Contreras, S., et al. 2017, MNRAS, 467, 2066, doi: [10.1093/mnras/stx243](https://doi.org/10.1093/mnras/stx243)
- Stewart, K. R., Brooks, A. M., Bullock, J. S., et al. 2013, ApJ, 769, 74, doi: [10.1088/0004-637X/769/1/74](https://doi.org/10.1088/0004-637X/769/1/74)
- Stewart, K. R., Maller, A. H., Oñorbe, J., et al. 2017, ApJ, 843, 47, doi: [10.3847/1538-4357/aa6dff](https://doi.org/10.3847/1538-4357/aa6dff)
- Swinbank, A. M., Harrison, C. M., Trayford, J., et al. 2017, MNRAS, 467, 3140, doi: [10.1093/mnras/stx201](https://doi.org/10.1093/mnras/stx201)
- Teklu, A. F., Remus, R.-S., Dolag, K., et al. 2015, ApJ, 812, 29, doi: [10.1088/0004-637X/812/1/29](https://doi.org/10.1088/0004-637X/812/1/29)
- Tenneti, A., Gnedin, N. Y., & Feng, Y. 2017, ApJ, 834, 169, doi: [10.3847/1538-4357/834/2/169](https://doi.org/10.3847/1538-4357/834/2/169)
- Tumlinson, J., Peebles, M. S., & Werk, J. K. 2017, ARA&A, 55, 389,  
doi: [10.1146/annurev-astro-091916-055240](https://doi.org/10.1146/annurev-astro-091916-055240)
- Turner, M. L., Schaye, J., Crain, R. A., et al. 2017, MNRAS, 471, 690, doi: [10.1093/mnras/stx1616](https://doi.org/10.1093/mnras/stx1616)
- Turner, M. L., Schaye, J., Steidel, C. C., Rudie, G. C., & Strom, A. L. 2014, MNRAS, 445, 794,  
doi: [10.1093/mnras/stu1801](https://doi.org/10.1093/mnras/stu1801)
- Übler, H., Naab, T., Oser, L., et al. 2014, MNRAS, 443, 2092, doi: [10.1093/mnras/stu1275](https://doi.org/10.1093/mnras/stu1275)
- van der Walt, S., Colbert, S. C., & Varoquaux, G. 2011, Computing in Science Engineering, 13, 22,  
doi: [10.1109/MCSE.2011.37](https://doi.org/10.1109/MCSE.2011.37)
- Vogelsberger, M., Genel, S., Sijacki, D., et al. 2013, MNRAS, 436, 3031, doi: [10.1093/mnras/stt1789](https://doi.org/10.1093/mnras/stt1789)
- Vogelsberger, M., Genel, S., Springel, V., et al. 2014a, Nature, 509, 177, doi: [10.1038/nature13316](https://doi.org/10.1038/nature13316)
- . 2014b, MNRAS, 444, 1518, doi: [10.1093/mnras/stu1536](https://doi.org/10.1093/mnras/stu1536)
- Weinberger, R., Springel, V., & Pakmor, R. 2019, arXiv e-prints, arXiv:1909.04667.  
<https://arxiv.org/abs/1909.04667>
- Weinberger, R., Springel, V., Hernquist, L., et al. 2017, MNRAS, 465, 3291, doi: [10.1093/mnras/stw2944](https://doi.org/10.1093/mnras/stw2944)
- Werk, J. K., Prochaska, J. X., Tumlinson, J., et al. 2014, ApJ, 792, 8, doi: [10.1088/0004-637X/792/1/8](https://doi.org/10.1088/0004-637X/792/1/8)
- Zabl, J., Bouché, N. F., Schroetter, I., et al. 2019, MNRAS, 485, 1961, doi: [10.1093/mnras/stz392](https://doi.org/10.1093/mnras/stz392)
- Zavala, J., Frenk, C. S., Bower, R., et al. 2016, MNRAS, 460, 4466, doi: [10.1093/mnras/stw1286](https://doi.org/10.1093/mnras/stw1286)
- Zjupa, J., & Springel, V. 2017, MNRAS, 466, 1625,  
doi: [10.1093/mnras/stw2945](https://doi.org/10.1093/mnras/stw2945)